Chapter 8

Decoration of a (111) Step at Pd(100) by Oxygen Atoms

As prominent defects at solid surfaces atomic steps are commonly perceived as playing some kind of special, if not decisive role for the surface properties or function in materials science applications. When it comes to the interaction with a reactive environment, steps are viewed as providing particularly active sites which can have a pronounced effect on the catalytic activity or act as nucleation centers for adsorbate-induced morphological transitions with oxide formation or corrosion in our oxygen-rich atmosphere as well-known examples. When aiming to qualify this role at the atomic scale an important first task is to identify the structure and composition at the step edge under realistic gas-phase conditions. On the modeling side, the first-principles atomistic thermodynamics approach [67] has brought considerable progress to this end for ideal low-index surfaces. In its prevalent form, this approach compares the stability of a variety of structural models in contact with a given gas-phase reservoir. Extending it to the study of steps depends then only on the ability to perform the underlying electronic structure calculations for corresponding structural models. For metal surfaces, one viable route to this is to resort to supercell geometries for vicinal surfaces, *i.e.* to compute periodic arrays of steps that can be suitably cast into a periodic boundary condition framework. Unfortunately, the high computational cost connected to such inherently large supercell calculations severely limits both the accessible surface unit-cell sizes and total number of structural models that can be computed. This prevents to date a proper exploration of the huge configurational space of possible step structures and allows at best for approximate treatments of entropic effects at elevated temperatures.

In this chapter we address these limitations by suitably combining the thermodynamic approach with a first-principles parameterized lattice-gas Hamiltonian (LGH) [67]. The concept is illustrated with the application to the on-surface oxygen adsorption at Pd(100), and there specifically to the decoration of close-packed (111) steps in an oxygen atmosphere. In Chapter 7 we proved that the binding properties at the center of (100) terraces of Pd(117) are little disturbed by the neighboring steps. Then

we employ large-scale density-functional theory (DFT) calculations for corresponding low-index O-Pd(100) and vicinal O-Pd(117) to determine the lateral interactions between adsorbates at the (100) terrace sites and at sites close to or at a (111) step. In a first stage the resulting multi-site LGH is then used to generate a large pool of possible structural models with varying on-surface O content. Within the thermodynamic framework the stability of these models is evaluated for a wide range of gas-phase conditions and compared to known more complex O-induced reconstructions at the low-index surface, namely an ultrathin $(\sqrt{5} \times \sqrt{5})R27^\circ$ (henceforth simply termed $\sqrt{5}$) surface oxide) and thick bulk-like PdO films [90, 91]. Intriguingly, this identifies a distinct range of O chemical potentials where a characteristic zigzag step decoration is most stable. Explicitly accounting for the configurational entropy we confirm with grand-canonical Monte Carlo (GCMC) simulations that this ordered structure is indeed stable up to quite elevated temperatures, in fact up to even higher temperatures than the concurrent ordered adsorbate structure at the Pd(100) terrace. At near atmospheric pressures such temperatures around and above 1000 K are representative for catalytic applications like the high-temperature combustion of methane [136], for which our study thus provides first insight into the structure and composition at a prominent defect on the working surface.

8.1 Computational Details

8.1.1 Total Energy Calculations

Again, we employ the **WIEN2k** code based on FP-(L)APW+lo, using GGA-PBE as the exchange-correlation factional, for the total energy calculations of various ordered oxygen structures at Pd(117) (see Appendix F). All surface structures are modeled in a supercell geometry, employing full-relaxed symmetric slabs (with O adsorption on both sides of the slab) consisting of 23 Pd(117) layers with an optimized bulk lattice constant of a= 3.947 Å. A minimum vacuum region of 12 Å ensures the decoupling of consecutive slabs. The (L)APW+lo basis set are listed as following: $R_{\mathrm{MT}}^{\mathrm{Pd}}$=2.1 bohr, $R_{\mathrm{MT}}^{\mathrm{O}}$=1.1 bohr, wave function expansion inside the muffin tin spheres up to $l_{\mathrm{max}}^{\mathrm{wf}}$=12, and potential expansion up to $l_{\mathrm{max}}^{\mathrm{pot}}$=6. The energy cutoff for the plane wave representation in the interstitial region between muffin tin spheres was $E_{\mathrm{max}}^{\mathrm{wf}}$=20 Ry for the wave functions and $E_{\mathrm{max}}^{\mathrm{pot}}$=196 Ry for the potential. Monkhorst-Pack (MP) grids were used for the Brillouin zone integrations. Specially, we use a (3×12×1) [1] for the calculation of the Pd(117)(1×1) surface unit cell. For the larger surface cells, care was taken to keep the reciprocal space point sampling identical by appropriately reducing the employed k-meshes, *e.g.* the k-meshes are changed to (3×6×1) and (3×4×1) for Pd(117)(1 × 2) and Pd(117)(1 × 3) surface unit-cell respectively. The total energy of the isolated O_2 molecule is obtained just as in Chapter 4.

[1] The k-mesh used in this chapter is different to the k-mesh in Chapter 7, which was $(6 \times 10 \times 1)$, for reasons which will be detailed below.

In order to explicitly account for the different hollow sites (Sh2, Sh1, Thu, Thc and Thl) at Pd(117), instead of using the average binding energy as in Eq. 4.10, we are going to use the total binding energy to do the comparison, and extract the lateral interactions. The total binding energy is defined as,

$$E_{\mathrm{b}}^{\mathrm{tot}} = -\frac{1}{2}\left[E_{\mathrm{O/Pd(117)}}^{\mathrm{total}} - E_{\mathrm{Pd(117)}}^{\mathrm{total}} - \frac{N_{\mathrm{O}}}{2}E_{\mathrm{O_2(gas)}}^{\mathrm{total}}\right] \quad , \tag{8.1}$$

where N_{O} is the total number of oxygen atoms in the supercell. $E_{\mathrm{O/Pd(117)}}^{\mathrm{total}}$, $E_{\mathrm{Pd(117)}}^{\mathrm{total}}$ and $E_{\mathrm{O_2(gas)}}^{\mathrm{total}}$ are the total energy of the adsorption system, of the corresponding clean system and of an isolated oxygen molecule, respectively. And the factor $\frac{1}{2}$ accounts for the fact that oxygen atoms adsorb at both sides of the symmetric slab.

8.1.2 Lattice-gas Hamiltonian for O-Pd(117)

Within the LGH approach, the free binding energy of any O-Pd(117) configuration can be written as the following cluster expansion formula,

$$F_{\mathrm{b}}^{\mathrm{tot}} = \sum_{i}^{\mathrm{site}} F_i^{\mathrm{on-site}} n_i + \sum_{l=1}^{\mathrm{r}} \sum_{(i<j)_l}^{\mathrm{site}} V_{l,\mathrm{p}}^{(i,j)} n_i n_j + \sum_{m=1}^{\mathrm{q}} \sum_{(i<j<k)_m}^{\mathrm{site}} V_{m,\mathrm{t}}^{(i,j,k)} n_i n_j n_k + \ldots \quad , \tag{8.2}$$

where $F_i^{\mathrm{on-site}}$ is the free energy of an isolated oxygen at site i, and for simplicity, we use 1, 2, 3, 4, and 5 to distinguish Thu, Thc, Thl, Sh2 and Sh1, the five hollow sites, respectively. For the nomenclatures of pair ($V_{l,\mathrm{p}}^{(i,j)}$) and triple ($V_{m,\mathrm{t}}^{(i,j,k)}$) interactions, the subscripts have the same meaning as the CE on the Pd(100) surface (Fig. 6.1): the lth pair interaction, and the mth triple interaction; and the superscripts indicate the pair interaction involves two sites i and j, and the trio interaction involves three sites i, j and k. The value of $n_{i,(j,k)}$ is 1 or 0 if the site $i,(j,k)$ is occupied or empty. The sum labels $(i<j)_l$ [or $(i<j<k)_m$] indicate that the sums run over all pairs of sites (ij) (and three sites (ijk)) that are separated by the l (or m) lateral figure, and the summation is done such, that each pair (or trio) of occupied sites contributes exactly once to the lattice energy.

We consider pair interactions between any combination of sites up to distances that correspond to the third nearest neighbor (NN) shell, as well as the most compact many-body interactions in form of trio interactions between any three site combination within a second NN shell distance. The resulting 70 inequivalent lateral interaction figures compiled in Fig. 8.1. As we mentioned the lateral interaction figure nomenclature contains the information of which kind interaction it is and which sites are involved. Taking $V_{2\mathrm{p}}^{12}$ as an example, the subscript 2p indicates this is a second nearest neighbor (2NN) pair interaction, and the superscript 12 indicates that this 2NN interaction is between Thu (1) and Thc (2) sites. Different to the Pd(100) surface, the present (111) steps divide the (100) surface into upper terraces and lower terraces.

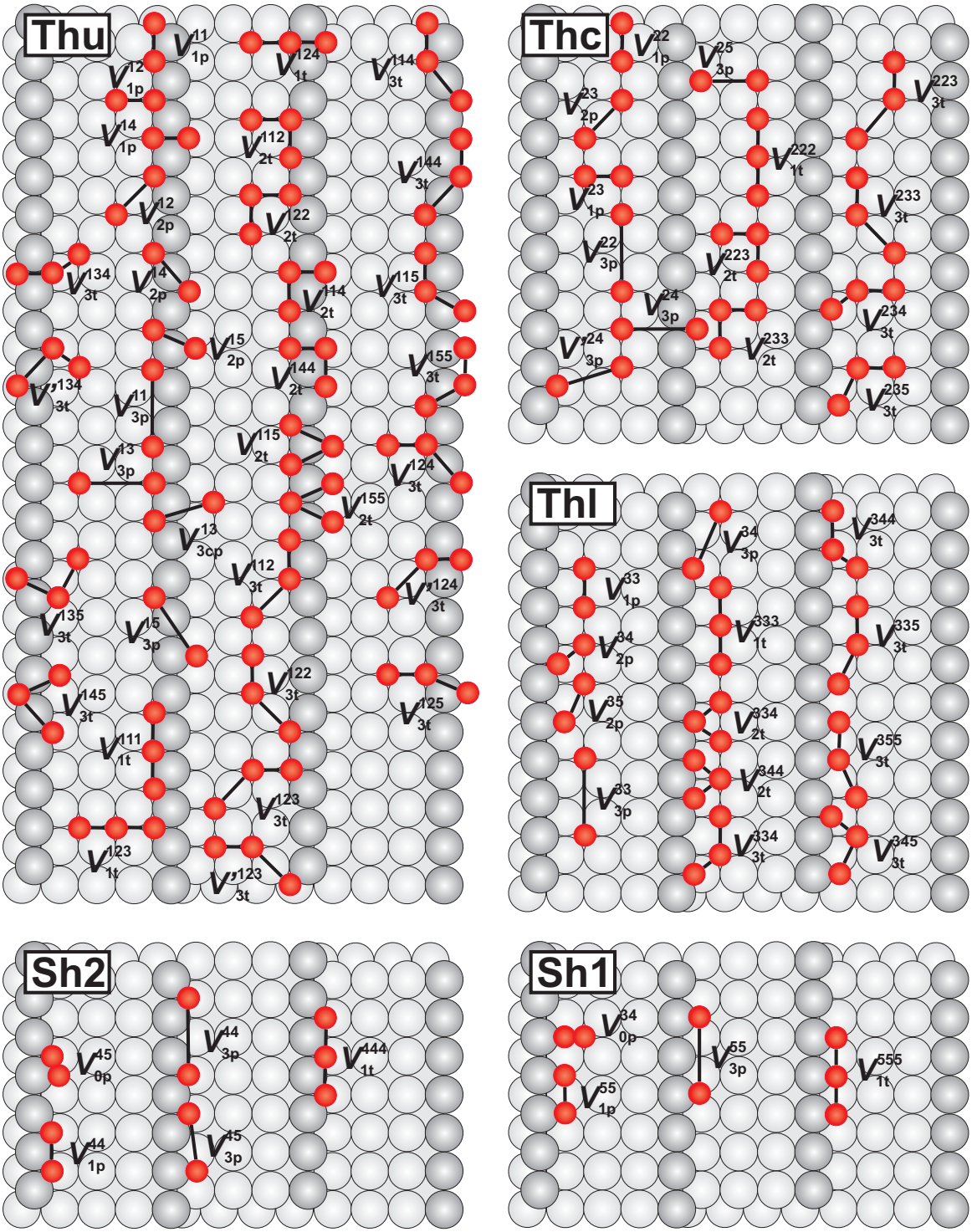

Figure 8.1: 70 step-influenced lateral interaction figures, including up to 3rd NN pair interactions and compact trios up to 2nd NN interactions. Light grey spheres represent Pd atoms, grey spheres Pd step atoms, and small dark (red) spheres O atoms. See text for the explanation nomenclature.

Table 8.1: Total binding energies of one oxygen atom at different sites in Pd(117)(1×1), (1×2) and (1×3) cells. Due to the different k-meshes, the binding energies in this table are slightly different to the ones in Table 7.5. The labels in parenthesis correspond to the names of the structures in Appendix F. (Unit: meV)

	Sh2	Sh1	Thu	Thc	Thl
1O−Pd(1×1)	953	845	876	819	595
	(V7-4)	(V7-5)	(V7-1)	(V7-2)	(V7-3)
1O−Pd(1×2)	1242	1073	1308	1279	1012
	(V7-16)	(V7-17)	(V7-13)	(V7-14)	(V7-15)
1O−Pd(1×3)	1286	1106	1265	1264	1009
	(V7-50)	(V7-51)	(V7-47)	(V7-48)	(V7-49)

This gives rise to additional lateral interactions across the (111) steps, like $V_{3\mathrm{cp}}^{13}$ (the pair interaction between Thu and Thl sites at consecutive (100) terraces). Due to the finite width of the terraces at Pd(117), there are furthermore interaction figures like $V_{1\mathrm{t}}^{123}$ that span across the entire terrace and involve both Thu sites at the upper edge and Thl sites at the lower step edge of the step. Such interaction figures will never be used in the LGH simulations with very large terrace widths presented below. However, in order to extract meaningful values for the other interaction figures from the Pd(117) DFT data, they need to be accounted for. Based on Eq. 8.2 and Fig. 8.1, the cluster expansion of each configuration is presented at the right side of each structure in the Appendix F.

8.2 First-principles Lattice-gas Hamiltonian for O at Pd(117)

8.2.1 Energetics for O−Pd(117)

The total binding energies of various ordered configurations of oxygen adsorption at Pd(117) computed within our DFT approach are also compiled in Appendix F. Table 8.1 collects just the binding energies of one oxygen atom at different sites in the Pd(117)(1×1), (1×2) and (1×3) cells. The binding energies of one oxygen atom at the (100) terraces in a Pd(117)(1×3) supercell, Thu and Thc sites, are degenerate, 1265 and 1264 meV, and they are quite similar to the binding energy of an isolated oxygen atom at the ideal Pd(100) surface, 1249 meV. This energetic value further supports the conclusion in Chapter 7, that the binding properties at the center of the (100) terraces of Pd(117) are only little different to oxygen at the Pd(100) surface, and are little disturbed by the neighboring steps. While for Sh2 and Sh1 or Thl, *i.e.* positions that are at the (111) steps or near to the steps, the oxygen binding

energetics is much different to O-Pd(100) due to the influence of the (111) steps.

All relaxed O-Pd(117) structures were carefully examined, and in some high coverage configurations the adsorbed O atoms induce large bucklings of the surrounding Pd atoms, so as to relax below the surface. Since this is not the physics of on-surface adsorption that we want to describe with the LGH, such configurations were − similarly to the procedure in Chapter 6 − excluded from the input data set.

Moreover, in configurations including the $V_{0\mathrm{p}}^{35}$ or $V_{0\mathrm{p}}^{45}$ lateral figure (Fig. 8.1), the oxygen atoms at Thl or Sh1 sites directly relaxed to the nearest hollow sites along the (100) terraces. This reflects very large repulsive interactions between O atoms at such short distances, which we correspondingly model in the LGH by setting $V_{0\mathrm{p}}^{35}$ or $V_{0\mathrm{p}}^{45}$ to infinite repulsion. This leaves a total of 105 DFT structures (see Appendix F) to obtain the lateral interactions (Fig. 8.1) at the (111) step region.

8.2.2 Lateral Interactions for O−Pd(117)

As we discussed in Chapter 6, whether or not including the on-site energy into the fitting group does not affect the final results. From Table 8.1, we deduce that the (1×3) cell is large enough to avoid all significant lateral interactions shown in Fig. 8.1, and we therefore take the binding energies of 1O-Thu-Pd(117)(1×3)(V7-13 in Appendix F), 1O-Thc-Pd(117)(1×3)(V7-14 in Appendix F), 1O-Thl-Pd(117)(1×3)(V7-15 in Appendix F), 1O-Sh2-Pd(117)(1×3)(V7-16 in Appendix F) and 1O-Sh1-Pd(117)(1×3)(V7-17 in Appendix F) as the on-site energies for the Thu, Thc, Thl, Sh2, and Sh1 sites, respectively.

Excluding these 5 on-site structures, the remaining 68 lateral interactions are then determined by least-squares fitting to the remaining 100 DFT ordered structures, following the same procedure outlined in Chapter 6. Table 8.2 summarizes the thereby obtained interaction values. We again calculate the LOO-CV score (Eq. 5.12) as a first indication of the reliability of the resulting LGH expansion. The CV score is 29 meV/O atom, which provides a measure for the average accuracy with which the LGH can predict the energetics of adatom configurations not included in the fitting procedure. There are a number of interaction figures in the set for Pd(117) that have a direct equivalent at the ideal Pd(100) surface. This concerns all interactions between the 3 different hollow sites Thu, Thc and Thl. Supporting our approach we find the interactions that only involve the Thc sites (pairs: $V_{1\mathrm{p}}^{22}$, $V_{3\mathrm{p}}^{22}$. trios: $V_{1\mathrm{t}}^{222}$) to be very similar to these parameters extracted in the LGH expansion at the ideal Pd(100) surface. This shows that not only the on-site energy, but also the lateral interactions of this site in the middle of the (100) terrace are already little disturbed by the presence of the neighboring steps. Interestingly, the same similarity holds also for all interactions involving the Thu site at the upper rim of the step edge. Also here, we extract pair interactions and trio interactions that are within 30 meV identical to those between hollow sites at Pd(100). Effectively, this thus leaves three adsorption sites that are noticeably affected by the step, the two step sites Sh1 and Sh2, and the fourfold site Thl at the lower rim of the step edge.

Table 8.2: Extracted on-site energies at Thu, Thc, Thl, Sh2 and Sh1 sites, and lateral interactions as represented in Fig. 8.1. (Unit: meV)

On-site	$E_{\mathrm{Thu}}^{\mathrm{on-site}}$	$E_{\mathrm{Thc}}^{\mathrm{on-site}}$	$E_{\mathrm{Thl}}^{\mathrm{on-site}}$	$E_{\mathrm{Sh2}}^{\mathrm{on-site}}$	$E_{\mathrm{Sh1}}^{\mathrm{on-site}}$
(meV)	1265	1264	1009	1286	1106

pair	$V_{1\mathrm{p}}^{11}$	$V_{1\mathrm{p}}^{12}$	$V_{1\mathrm{p}}^{14}$	$V_{2\mathrm{p}}^{12}$	$V_{2\mathrm{p}}^{14}$	$V_{2\mathrm{p}}^{15}$	$V_{3\mathrm{p}}^{11}$	$V_{3\mathrm{p}}^{13}$	$V_{3\mathrm{cp}}^{13}$	$V_{3\mathrm{p}}^{15}$
(meV)	-299	-283	-420	-90	133	41	41	80	-49	-10
pair	$V_{1\mathrm{p}}^{22}$	$V_{1\mathrm{p}}^{23}$	$V_{2\mathrm{p}}^{23}$	$V_{3\mathrm{p}}^{22}$	$V_{3\mathrm{p}}^{24}$	$V'^{24}_{3\mathrm{p}}$	$V_{3\mathrm{p}}^{25}$	$V_{1\mathrm{p}}^{33}$	$V_{2\mathrm{p}}^{34}$	$V_{2\mathrm{p}}^{35}$
(meV)	-298	-413	-150	20	7	-11	23	-138	-212	-119
pair	$V_{3\mathrm{p}}^{33}$	$V_{3\mathrm{p}}^{34}$	$V_{1\mathrm{p}}^{44}$	$V_{3\mathrm{p}}^{44}$	$V_{3\mathrm{p}}^{45}$	$V_{1\mathrm{p}}^{55}$	$V_{3\mathrm{p}}^{55}$			
(meV)	13	-21	-274	-53	-70	-19	-66			

trio	$V_{1\mathrm{t}}^{111}$	$V_{1\mathrm{t}}^{123}$	$V_{1\mathrm{t}}^{124}$	$V_{2\mathrm{t}}^{112}$	$V_{2\mathrm{t}}^{122}$	$V_{2\mathrm{t}}^{114}$	$V_{2\mathrm{t}}^{144}$	$V_{2\mathrm{t}}^{115}$	$V_{2\mathrm{t}}^{155}$
(meV)	-145	-155	-258	63	52	93	94	-59	84
trio	$V_{3\mathrm{t}}^{112}$	$V_{3\mathrm{t}}^{122}$	$V_{3\mathrm{t}}^{123}$	$V'^{123}_{3\mathrm{t}}$	$V_{3\mathrm{t}}^{114}$	$V_{3\mathrm{t}}^{144}$	$V_{3\mathrm{t}}^{115}$	$V_{3\mathrm{t}}^{155}$	$V_{3\mathrm{t}}^{124}$
(meV)	-14	-16	-38	-26	2	18	-40	-35	-28
trio	$V'^{124}_{3\mathrm{t}}$	$V_{3\mathrm{t}}^{125}$	$V_{3\mathrm{t}}^{134}$	$V'^{134}_{3\mathrm{t}}$	$V_{3\mathrm{t}}^{135}$	$V_{3\mathrm{t}}^{145}$	$V_{1\mathrm{t}}^{222}$	$V_{2\mathrm{t}}^{223}$	$V_{2\mathrm{t}}^{233}$
(meV)	-98	-144	-80	-78	-61	62	-166	116	125
trio	$V_{3\mathrm{t}}^{223}$	$V_{3\mathrm{t}}^{233}$	$V_{3\mathrm{t}}^{234}$	$V_{3\mathrm{t}}^{235}$	$V_{1\mathrm{t}}^{333}$	$V_{2\mathrm{t}}^{334}$	$V_{2\mathrm{t}}^{344}$	$V_{3\mathrm{t}}^{334}$	$V_{3\mathrm{t}}^{344}$
(meV)	-30	-53	128	-72	-285	131	8	-45	89
trio	$V_{3\mathrm{t}}^{335}$	$V_{3\mathrm{t}}^{355}$	$V_{3\mathrm{t}}^{345}$	$V_{1\mathrm{t}}^{444}$	$V_{1\mathrm{t}}^{555}$				
(meV)	-79	-28	73	-5	-66				

Table 8.3: Comparison of equivalent lateral interaction figures involving Thu and Thc sites at O-Pd(117) and the hollow sites at O-Pd(100). The additional data in the parentheses are the corresponding values. (Unit: meV)

O-Pd(100)	O-Pd(117)					
$V_{1\mathrm{p}}$ (-292)	$V_{1\mathrm{p}}^{11}$	(-299)	$V_{1\mathrm{p}}^{22}$	(-298)	$V_{1\mathrm{p}}^{12}$	(-283)
$V_{2\mathrm{p}}$ (-90)	$V_{2\mathrm{p}}^{12}$	(-90)				
$V_{3\mathrm{p}}$ (50)	$V_{3\mathrm{p}}^{11}$	(41)	$V_{3\mathrm{p}}^{22}$	(20)		
$V_{1\mathrm{t}}$ (-168)	$V_{1\mathrm{t}}^{111}$	(-145)	$V_{1\mathrm{t}}^{222}$	(-166)		
$V_{2\mathrm{t}}$ (60)	$V_{2\mathrm{t}}^{112}$	(63)	$V_{2\mathrm{t}}^{122}$	(52)		
$V_{3\mathrm{t}}$ (-48)	$V_{3\mathrm{t}}^{112}$	(-14)	$V_{3\mathrm{t}}^{122}$	(-16)		

8.2.3 Vibrational Contribution to the Lateral Interactions

The energetic parameters in Eq. 8.2 comprise total and vibrational free energy contributions. In addition to the total energy based lateral interactions discussed in the last section, we also account for the vibrational contribution in an approximate way, following the procedure detailed in Chapter 6. This means that we account for the leading vibrational contribution which gets concentrated in the on-site energy by adding the ZPE correction due to the change of the O_2 stretch frequency to the O-substrate stretch frequency (Eq. 6.7).

In order to obtain an estimate of this stretch mode we focus on configurations with one O atom at the Sh2 site in a (1×2) cell (V7-16 in Appendix F), and one O atom at the Thu site in a (1×2) cell (V7-13 in Appendix F), as well as on one configuration involving two O atoms at Thu and Sh2 sites in a (1×2) cell (V7-23 in Appendix F). In line with the conclusions taken in Chapter 6 we obtain only small differences in the stretch modes of both the step atom (Sh2) and the terrace site atom (Thu) at the two computed coverages ($\sim$ 5 meV difference each). On the other hand, the modes at the 3-fold step and 4-fold hollow sites are slightly different ($\sim$ 20 meV at the step and $\sim$ 30 meV at the terrace). Correspondingly, we account for the vibrational contribution to zeroth order by correcting the on-site energies at the step sites (Sh1 and Sh2) by 20 meV and correcting the on-site energies at the terrace sites (Thu, Thc, Thl) by 30 meV.

8.2.4 Validation by Direct Enumeration

In the work on the ordering behavior of oxygen at the Pd(100) surface in Chapter 6, there was only one kind of important adsorption site, the hollow site. Focusing on the order-disorder transition at constant number of adsorbed O atoms, we could there focus on the formation energy, Eq. 5.13 to check on the consistency of the DFT input structures and the ground-state structures predicted by the LGH via direct enumeration, see Chapter 6.2.2. In this Chapter we are more interested in the ordering behavior in a grand-canonical ensemble, *i.e.* allowing for particle exchange with the surrounding gas-phase. We therefore use here the Gibbs free energy of adsorption defined as Eq. 8.3 to validate our O-Pd(117) DFT input data set.

$$\begin{aligned} \Delta G(\Delta\mu_{\mathrm{O}}) &\approx -\frac{1}{2A}(E^{\mathrm{total}}_{\mathrm{O/Pd(117)}} - E^{\mathrm{total}}_{\mathrm{Pd(117)}} - \frac{N_{\mathrm{O}}}{2}E^{\mathrm{total}}_{\mathrm{O_2(gas)}} - N_{\mathrm{O}}\Delta\mu_{\mathrm{O}}) \\ &= \frac{1}{2A}(2E^{\mathrm{tot}}_{\mathrm{b}} + N_{\mathrm{O}}\Delta\mu_{\mathrm{O}}) \quad , \end{aligned} \tag{8.3}$$

where $E^{\mathrm{total}}_{\mathrm{O/Pd(117)}}$, $E^{\mathrm{total}}_{\mathrm{Pd(117)}}$, $E^{\mathrm{total}}_{\mathrm{O_2(gas)}}$, and $E^{\mathrm{tot}}_{\mathrm{b}}$ have the same meaning as in Eq. 8.1. $\Delta\mu_{\mathrm{O}}$ is the oxygen chemical potential, A is the surface unit area, and N_{O} is the total number of the oxygen atoms in the supercell.

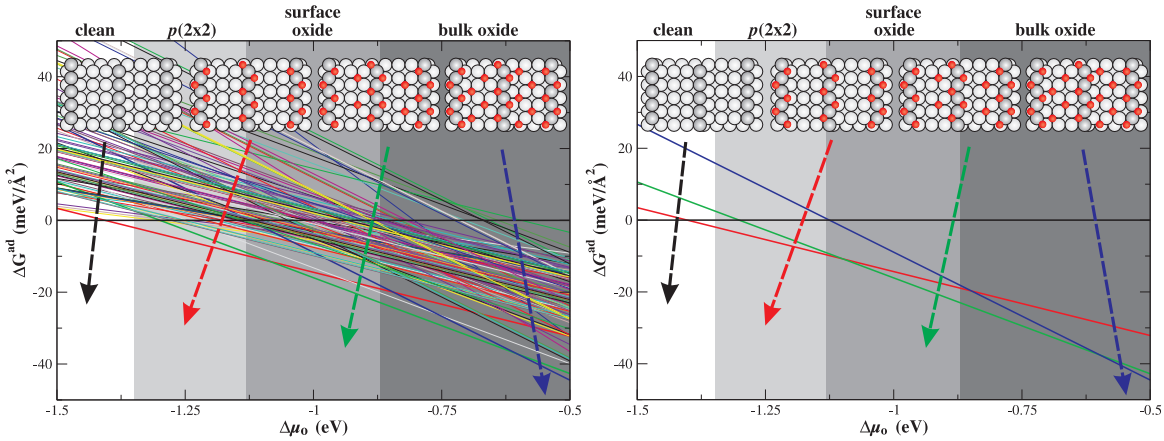

Figure 8.2: Phase diagrams of DFT calculations (left panel) and of corresponding DE data (right panel). The structures on the top of each panel show the most stable structures in different oxygen chemical as obtained in previous work (ref. [60]). In the DE phase diagram, we only show the lines of the most stable configurations.

Using all DFT structures to construct the thermodynamic phase diagram we compare this to the phase diagram obtained when directly enumerating any ordered structure that can be produced in a Pd(117)(1×3) cell with the LGH energetics. Similar to Chapter 6 we did this in an iterative fashion, by starting with a small group of DFT input structures to construct the LGH. Using this LGH for the DE method to obtain ΔG for all arbitrary configurations within a (1×3) cell, we then plotted the DE thermodynamic phase diagram, and compared it to the DFT phase diagram. If new configurations showed up, they were calculated by DFT. Then, including this new DFT data to get a new LGH, the DE was redone until DFT and DE phase diagrams agreed with each other.

Finally, the left and right panels in Fig. 8.2 illustrate the DFT phase diagram and the direct enumeration phase diagram using the the final LGH presented in Sections 8.2.1 and 8.2.2, respectively. The nice agreement between the two phase diagrams indicates that our DFT input set is able to parameterize a LGH that gives a sequence of most stable structures at different $\Delta\mu_O$ that is consistent with the original DFT input set. At this stage we content ourselves with this similarity and defer a discussion of the physics of this phase diagram to Section 8.3.2 below.

8.2.5 Treating the Boundary for Surfaces with Wider Terrace Width

The parameterization of the LGH was exclusively done using DFT data for the Pd(117) surface. If one wants to employ this LGH to also simulate the ordering

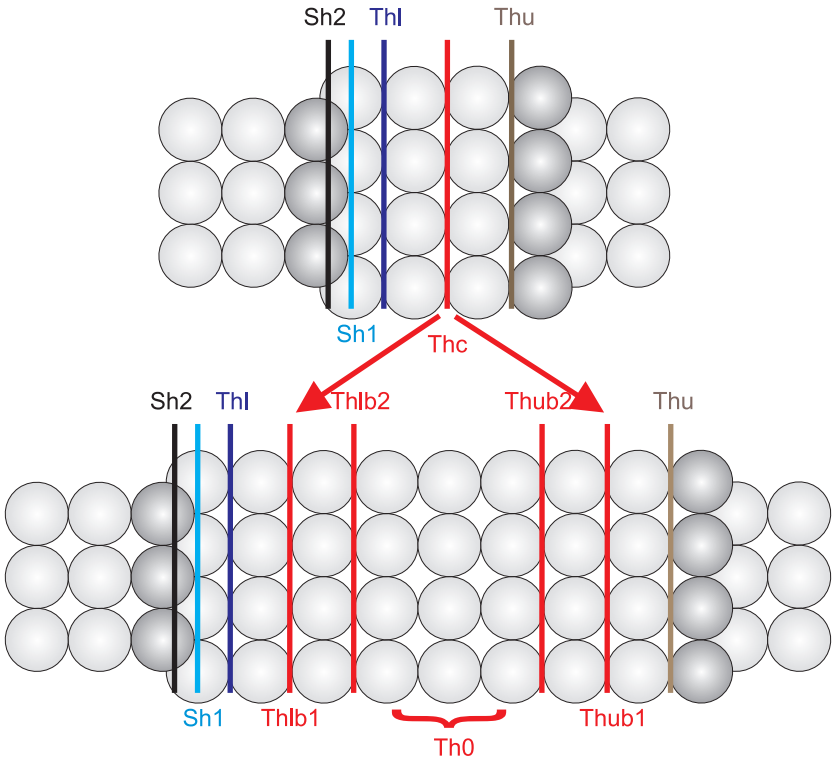

Figure 8.3: Schematic top view of the sites at the 4 atomic row (100) terraces at (117) and the site types at wider terrace width. Sh2, Sh1, Thu, Thc and Thl have the same meaning as usual, whereas on a wider (100) terrace, the Thc sites have to be divided into different sites, Thlb1, Thlb2, Th0, Thub1, and Thub2, according to their distance to the step. For the presently employed range of lateral interactions (up to 3rd NN pairs) all sites marked as Th0 are indistinguishable from hollow sites at a (100) surface. "b" indicates the boundary between Thl and Th0, or between Thu and Th0.

behavior of O atoms at vicinals with a wider terrace width − or ultimately the ordering behavior of O atoms at an isolated step at Pd(100) − one further issue needs to be addressed. As illustrated in Fig. 8.3 a wider terrace width gives rise to two additional rows of sites that for the employed pool of short-ranged interactions can have lateral interactions that are neither covered by the (117)-derived interactions, nor the (100)-derived interactions. If we take for example the Thl sites, the farthest reaching interaction in form of the third NN pair interaction reaches to the sites Thlb2, *i.e.* one needs an interaction $V_{3\mathrm{p}}$ Thl-Thlb2. On the other hand, what we only have are either the interaction $V_{3\mathrm{p}}$ from Pd(100), which is not entirely correct since the Th0 site is not a terrace site. Or we have the interaction $V_{3\mathrm{p}}^{13}$, which is neither entirely correct since the Thlb2 site is not a Thu site. Fortunately, as discussed before, in many cases the involved lateral interactions are very similar. What we therefore did in practice was to either always approximate the unknown boundary interactions by the equivalent interactions from the Pd(100) LGH, or to always approximate the unknown boundary interactions by the equivalent interactions from the (117) LGH. The obtained results

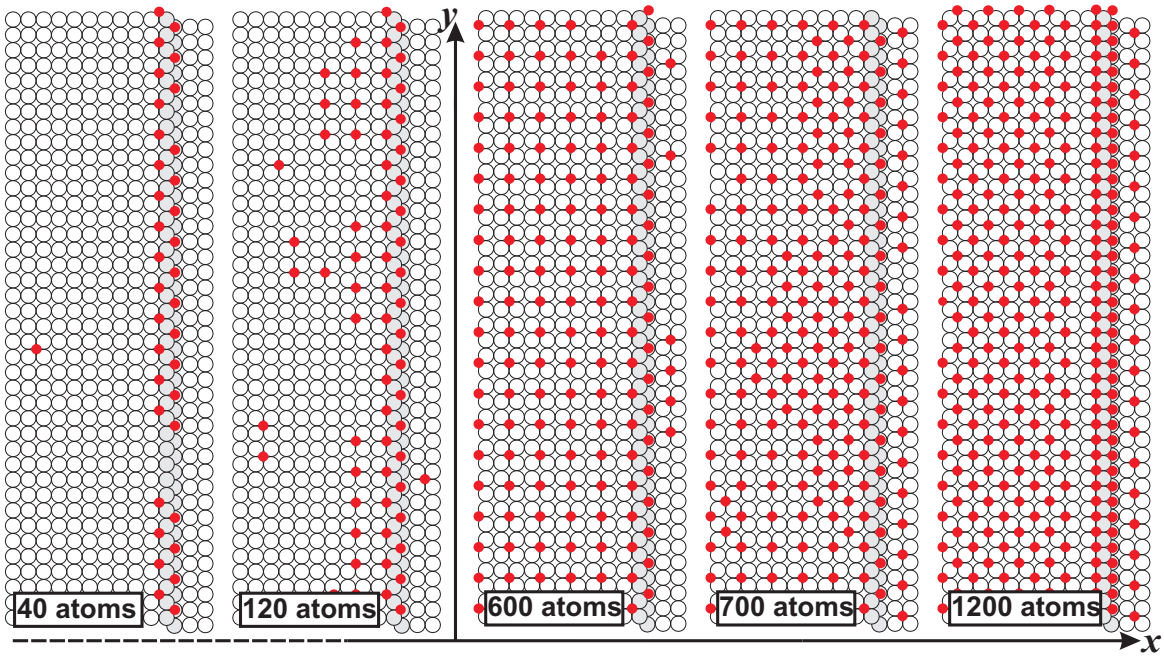

Figure 8.4: Schematic top views showing the results of simulated annealing runs with different number of oxygen atoms in $(60 \times 40)(100)$ cell with one (111) step inside. Shown are the results after the temperature quenching had reached room temperature (300 K). In order to save space, each panel only shows one (111) step (grey region) and 10 rows away from the (111) step at the (100) terrace. The two perpendicular lines are x and y directions. The additional data are the total number of oxygen atoms in the simulation cells.

were in both cases very similar so that we concentrate in the remainder of this chapter on presenting the results for the case, where the interactions in the boundary region were approximated with the values form the Pd(100) LGH.

8.3 Ordering Behavior of Oxygen Near a (111) Step at Pd(100)

8.3.1 Simulated Annealing Simulation: Identify Low-energy Step structures

In a first stage we exploit the low computational cost to evaluate the established first-principles multi-site LGH to extensively explore the huge configuration space and identify low-energy ordered step structures. This is achieved by simulated annealing runs in periodic boundary condition simulation cells containing (60×40) (100) surface unit-cells and one (111) step along the shorter cell axis (see Appendix D). For fixed and initially random O coverages ranging up to a half filling of all terrace hollow sites 10^8 MC steps are used to continuously quench from an initial temperature of

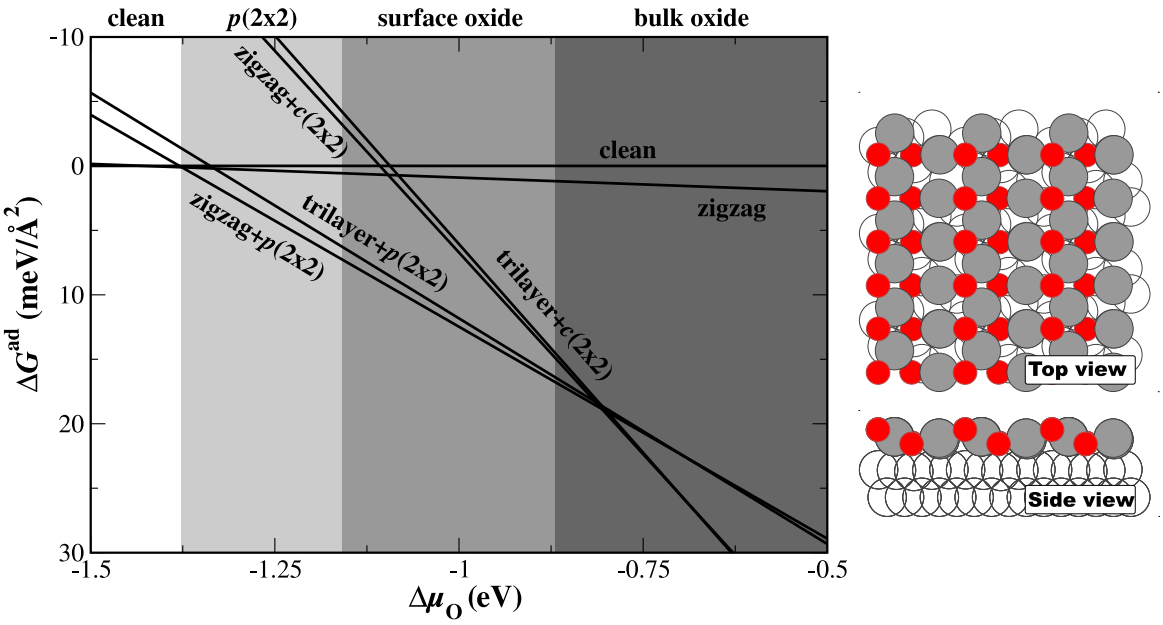

Figure 8.5: Computed Gibbs free energy of adsorption ΔG^{ad} for O adsorbate structures at a (111) step at Pd(100) and using the clean surface as zero reference (left panel). Using the nomenclature defined in Fig. 8.6 the labels refer to the structure at the step and at the neighboring terrace, *e.g.* zigzag+$p(2 \times 2)$ stands for a zigzag step decoration coexisting with the $p(2 \times 2)$ adsorbate ordering at the terrace. Additionally indicated by differently shaded backgrounds are the stability regions obtained for the ideal Pd(100) surface in previous work [58, 135], namely those of the $p(2 \times 2)$ overlayer, of the surface oxide structure (right panel) and of a thick bulk-like PdO film.

2000 K. Depending on the O content, these simulations unanimously lead to patches of increasing size of four distinct ordered structures that are schematically shown in Fig. 8.4 and 8.6. At the lowest coverages the O adatoms quickly decorate the Thu and Sh2 sites at the (111) step in a characteristic zigzag structure with (2×1) periodicity (the first left panel in Fig. 8.4). At increasing coverages domains of the experimentally well characterized $p(2 \times 2)$ overlayer [90] start to form at the (100) sites next to the upper edge of the fully zigzag decorated step (the second left panel in Fig. 8.4). After the $p(2 \times 2)$ extends over the whole (100) terrace, further adding oxygen atoms leads to the zigzag decorated step hand in hand with the $c(2 \times 2)$ domain (the second right panel in Fig. 8.4). Only once the O content in the simulation cell exceeds the one required to fully cover the entire terrace with the $c(2 \times 2)$ structure, does a further decoration of Thu and Sh2 step sites occur. This results in a (1x1) periodic step structure, which we henceforth term trilayer.

8.3.2 Stability of Zigzag Decorated Step

For the identified structural models we now account for the effect of a finite gas-phase environment through the atomistic thermodynamics approach [67]. Here, the surface

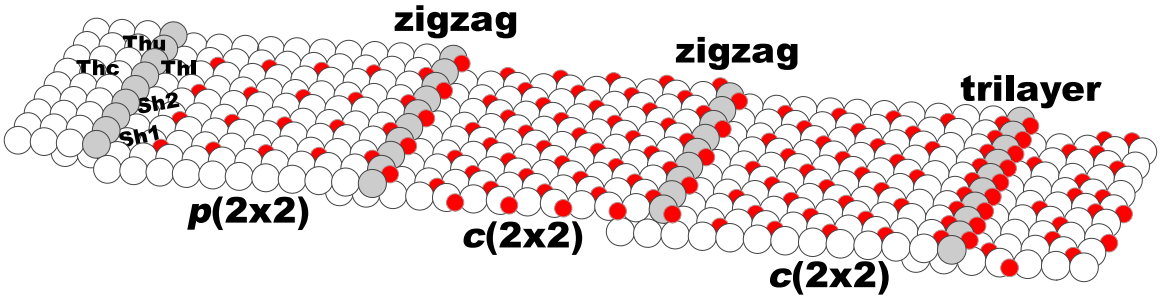

Figure 8.6: Schematic view of a Pd(100) surface with (111) steps. Shown are the five distinct adsorption sites considered in the first-principles lattice-gas Hamiltonian: The fourfold coordinated (100) hollow sites at the terraces (Thc), at the upper (Thu) and lower (Thl) rim of the step, as well as the two threefold (111) hollow sites at the step edge, one with a coordination to two step atoms (Sh2) and one with a coordination to one step atom (Sh1). Additionally represented are five characteristic ordered structures discussed in the text: A $p(2 \times 2)$ and a $c(2 \times 2)$ adsorbate phase at the (100) terrace, a zigzag structure where the step is decorated with O atoms in alternating Thu and Sh2 sites, and a trilayer structure where all Thu and Sh2 are occupied (Pd = large spheres, Pd step atoms = large dark spheres, O = small spheres).

is considered to be in equilibrium with an oxygen gas-phase reservoir characterized by a chemical potential $\Delta\mu_{\mathrm{O}}(T, p)$ summarizing the two-dimensional dependence on pressure p and temperature T. In its prevalent form this approach neglects the effect of configurational entropy at the surface and then simplifies to computing the Gibbs free energy of adsorption for any ordered structural model at any given $\Delta\mu_{\mathrm{O}}(T, p)$ from its corresponding binding free energy [55, 56]. This allows to readily compare the stability of most distinct structural models over a wide range of gas-phase conditions, and is thus ideally suited to also assess under which gas-phase conditions the surface structure and composition at the step is appropriately described by our on-surface LGH model. We correspondingly employ this approximate approach here not only to obtain a first understanding of the stability of the presented step models, but also to contrast this with the stability ranges of more complex O-rich phases identified previously for the ideal Pd(100) surface [58, 135]. Specifically, these are the $\sqrt{5}$ surface oxide structure (the right panel in Fig. 8.5), which corresponds to a sub-nanometer thin film of PdO(101) on the surface [91], and bulk PdO to represent thick bulk-like oxide films. The results are summarized in Fig. 8.5 and reveal a large stability range of the zigzag decoration of the (111) step, which over most of this range coexists with the $p(2 \times 2)$ adsorbate phase on the (100) terrace. The trilayer arrangement becomes only more favorable at quite elevated chemical potentials and coexists then directly with the denser $c(2 \times 2)$ overlayer on the terrace. In light of the also shown stability ranges of the oxidic phases at ideal Pd(100) we can therefore identify quite a range of gas-phase conditions ($-1.43\,\mathrm{eV} < \Delta\mu_{\mathrm{O}} < -1.16\,\mathrm{eV}$) that are not yet O-rich enough to induce oxide formation and where the zigzag step decoration is not just due to kinetics, but instead represents a thermodynamically stable phase in its own right.

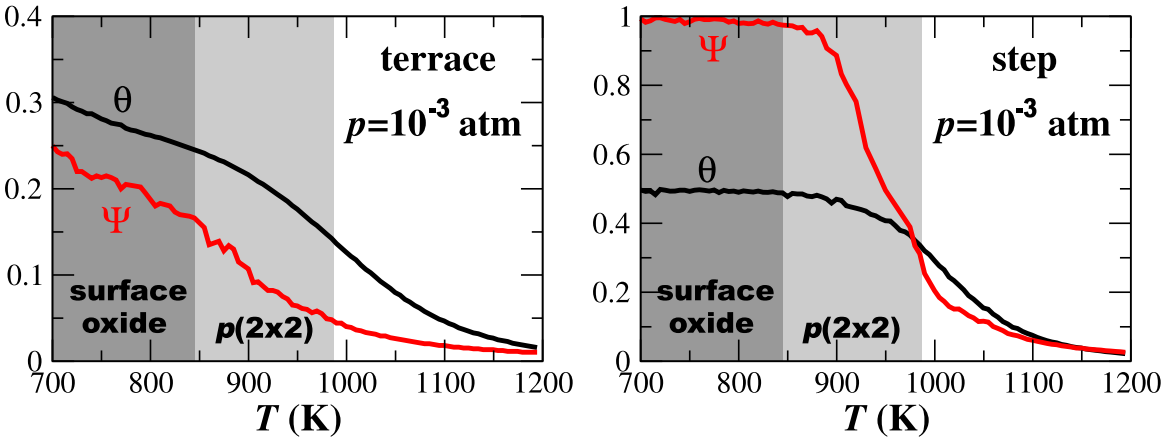

Figure 8.7: Average coverage (black lines) and order parameter (red lines) for the terrace (left panel) and step (left panel) sites as determined by grand-canonical MC simulations for a fixed oxygen pressure of 10^{-3} atm. The order parameters are sensitive to the lateral periodicities of the (2×1) zigzag step structure and the $p(2 \times 2)$ arrangement at the terrace, respectively. The coverages are normalized to the full occupation of all Sh2+Thu step sites and the full occupation of all hollow terrace sites. Vertical lines indicate the stability range as determined in Fig. 8.5. Equivalent results are obtained for simulations at $p = 10^{-5}$ and $p = 1$ atm, with corresponding variations of the critical temperatures of the order of 100 K.

In contrast, the elevated $\Delta\mu_O(T, p)$ at which the trilayer arrangement at the step becomes more favorable than the zigzag decoration fall well into the stability range of the oxidic surface reconstructions. This suggests an interpretation of the trilayer structure in form of a kinetic precursor in the oxide formation process, and in this respect it is intriguing to note that its geometric structure coincides in fact with one row of the $\sqrt{5}$ surface oxide (the right panel in Fig. 8.5).

At near atmospheric pressures the stability range of the zigzag step decoration ($-1.43\,\text{eV} < \Delta\mu_O < -1.16\,\text{eV}$) corresponds to rather elevated temperatures of the order of 1000 K [55, 56]. At such temperatures, configurational entropic effects can not be uncritically dismissed. We therefore scrutinize the insight provided by the approximate thermodynamic approach by fully accounting for such effects with grand-canonical MC simulations based on the first-principles LGH. In these simulations, the effect of the (111) step on the adsorbate ensemble in its vicinity is evaluated by separately monitoring the order and coverage for each row of sites (Eq. 5.29) parallel to the step edge using equivalent simulation cells as for the simulated annealing runs. Interestingly, the disturbance exerted by the step is found to be rather short ranged on the accuracy level of interest to this study. Already four atomic rows away from the immediate step edge the computed critical temperatures are to within ±50 K identical to those obtained at the ideal Pd(100) surface (Appendix D).

We correspondingly restrict the discussion on the ordering behavior directly at the step row itself, contrasting it with the ordering behavior at a row of ideal Pd(100)

hollow sites far away from the step. The results for a pressure $p = 10^{-3}$ atm are shown in Fig. 8.7. Since the prevalent ordered structures in the corresponding (T, p)-range are the $p(2 \times 2)$ at the terrace and the (2×1) zigzag decoration at the step order parameters that are sensitive to these lateral periodicities can be suitably employed to determine the critical temperature for the order-disorder transition at fixed oxygen pressure (Chapter 5: the order parameter for $p(2\times2)$ periodicity on terrace is Eq. 5.23 and the order parameter for the zigzag structure has the same formula as in Eq. 5.27). In addition to the GCMC results in Fig. 8.7, we also convert the thermodynamic oxygen chemical potentials of $p(2 \times 2)$-(100) (light grey block) and $\sqrt{5}$ surface oxide (grey block) into the temperatures at 10^{-3} atm. They are (987 K, 10^{-3} atm) for $p(2 \times 2)$ and (846 K, 10^{-3} atm) for the surface oxide.

From Fig. 8.7 we see that at the chosen pressure all temperatures below 846 K fall into the stability regime of the $\sqrt{5}$ surface oxide, which we cannot model with the present on-surface LGH. Focusing therefore on the temperatures above this limit we see that the stability range of the $p(2 \times 2)$ phase at the terrace predicted by the atomistic thermodynamics approach is an artifact of the neglected configurational entropy. In the GCMC simulations that explicitly account for this entropic contribution we indeed find a coverage of O atoms in hollow sites in this temperature range that corresponds to the coverage of the $p(2 \times 2)$ phase. However, over the entire temperature range above 846 K the order parameter has already decreased to small values, *i.e.* there is no long-range order at these temperatures anymore. The real population at the Pd(100) terraces is thus a low-coverage of disordered O atoms in hollow sites. This is much in contrast to the situation at the step, where a high order parameter indicates that the ordered zigzag structure is indeed stable even at these elevated temperatures. The order-disorder transition as reflected by the order parameter occurs only at temperatures around 950 K, where then also desorption of the on-surface oxygen atoms occurs.

8.4 Conclusion

Through a combination of first-principles statistical mechanics techniques we are therefore able to identify a wide range of environmental conditions, in which (111) steps at Pd(100) will be decorated by a characteristic zigzag oxygen structure. This includes near atmospheric pressures and temperatures around and above 1000 K, *i.e.* gas-phase conditions that are representative for an important catalytic process like the high-temperature combustion of methane, and Fig. 8.9 shows a schematic perspective view of the resulting surface structure and composition under these conditions. Due to the low energetic cost of the close-packed steps, this defect will be a frequent structural motif at the surface with corresponding potential influence on the function in such applications. In this respect it is interesting to notice that the same ordered zigzag O structure was recently characterized at the (111) steps of Pd(111) vicinals in the same range of oxygen chemical potentials, albeit at lower temperatures

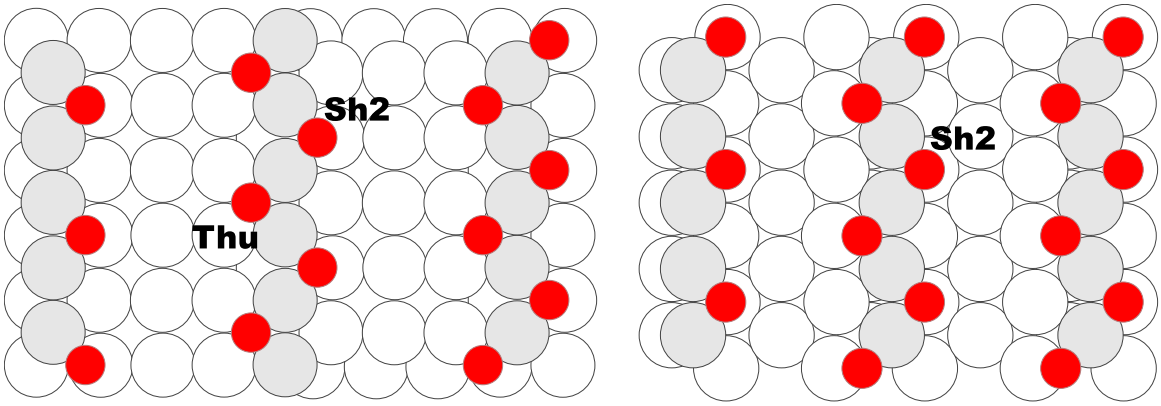

Figure 8.8: Two Pd vicinal structures used to calculate the O 1*s* surface-core level shifts for comparison. Left panel: the zigzag structure of O-Pd(117), which exhibits (111) steps and (100) terraces. Right panel: zigzag structure of O-Pd(221), which exhibits (111) steps and (111) terraces.

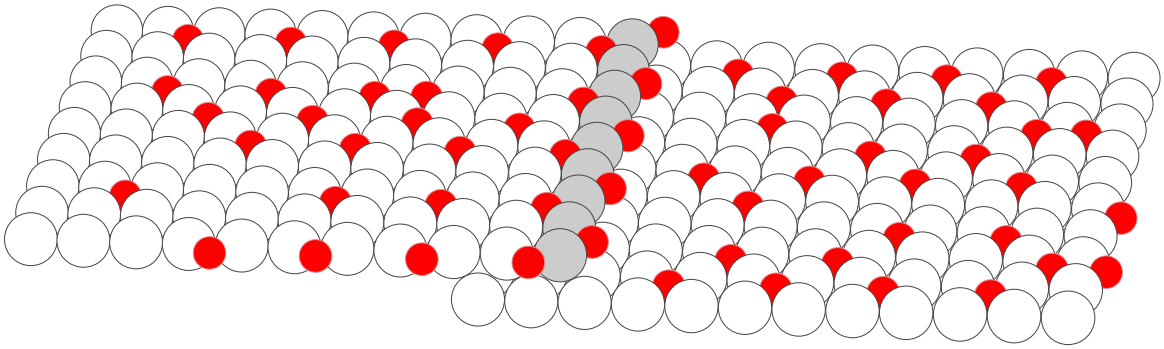

Figure 8.9: Schematic perspective view of the surface under gas-phase conditions representative of high-temperature methane combustion.

[137]. Using our LAPW/APW+lo DFT setup we compute initial and final state O 1*s* core level shifts [51] that are identical to within 40 meV for the O atoms adsorbed at the geometrically equivalent Sh2 step sites in the two structures (Fig. 8.8). Since core level shifts are a sensitive probe of the local bonding properties, this suggests highly similar reactivities of the oxygen atoms adsorbed at the decorated (111) steps at both prominent facets of Pd nanoparticles. If these oxygen atoms play a determining role for the catalytic function, this similarity would then provide an intriguing atomic-scale interpretation for the enigmatic structure insensitivity reported recently for the high-temperature methane combustion [136]. While our study focuses on establishing a first methodological access to determine the structure and composition of a prominent defect like atomic steps at surfaces exposed to realistic environments, this immediately exemplifies the far-reaching insight that this kind of first-principles

statistical mechanics approach can provide.